



Dmitry Balandin · Konstantin Barkalov ·  
Victor Gergel · Iosif Meyerov (Eds.)

# Mathematical Modeling and Supercomputer Technologies


20th International Conference, MMST 2020  
Nizhny Novgorod, Russia, November 23–27, 2020  
Revised Selected Papers

### *Editors*

Dmitry Balandin   
Lobachevsky State University of Nizhni  
Novgorod  
Nizhny Novgorod, Russia

Victor Gergel   
Lobachevsky State University of Nizhni  
Novgorod  
Nizhny Novgorod, Russia

Konstantin Barkalov   
Lobachevsky State University of Nizhni  
Novgorod  
Nizhny Novgorod, Russia

Iosif Meyerov   
Lobachevsky State University of Nizhni  
Novgorod  
Nizhny Novgorod, Russia

ISSN 1865-0929 ISSN 1865-0937 (electronic)  
Communications in Computer and Information Science  
ISBN 978-3-030-78758-5 ISBN 978-3-030-78759-2 (eBook)  
<https://doi.org/10.1007/978-3-030-78759-2>

© Springer Nature Switzerland AG 2021

This work is subject to copyright. All rights are reserved by the Publisher, whether the whole or part of the material is concerned, specifically the rights of translation, reprinting, reuse of illustrations, recitation, broadcasting, reproduction on microfilms or in any other physical way, and transmission or information storage and retrieval, electronic adaptation, computer software, or by similar or dissimilar methodology now known or hereafter developed.

The use of general descriptive names, registered names, trademarks, service marks, etc. in this publication does not imply, even in the absence of a specific statement, that such names are exempt from the relevant protective laws and regulations and therefore free for general use.

The publisher, the authors and the editors are safe to assume that the advice and information in this book are believed to be true and accurate at the date of publication. Neither the publisher nor the authors or the editors give a warranty, expressed or implied, with respect to the material contained herein or for any errors or omissions that may have been made. The publisher remains neutral with regard to jurisdictional claims in published maps and institutional affiliations.

This Springer imprint is published by the registered company Springer Nature Switzerland AG  
The registered company address is: Gewerbestrasse 11, 6330 Cham, Switzerland



# Methods for Simulation the Nonlinear Dynamics of Gyrotrons

Evgeny Semenov<sup>(✉)</sup> , Vladimir Zapevalov , and Andrey Zuev 

Federal Research Center Institute of Applied Physics of the Russian Academy of Sciences (IAP RAS), Nizhny Novgorod, Russia  
`semes@ipfran.ru`

**Abstract.** Determining the efficiency of high-power gyrotrons and studying operating regimes require solving self-consistent problems of the electron-wave interaction in the gyrotron cavity. Two mathematical models are considered: the stationary model that reduces to the Sturm—Liouville problem for the inhomogeneous string equation, and the time-depended model that combines the Schrödinger equation and equations of electron motion. The algorithms described in this paper are implemented in the code-package ANGEL (Analyzer of a Gyrating Electrons), which is used at IAP RAS and GYCOM Ltd. to analyze an electron-wave interaction in gyrotrons. The impact of ohmic losses in a terahertz gyrotron cavity on the efficiency and a stable single-mode operation is investigated. It is shown that a high fraction of ohmic losses can lead to disruption of the stable single-mode generation of terahertz gyrotrons operating at a high cyclotron harmonic.

**Keywords:** Inhomogeneous string equation · Schrödinger equation · Crank—Nicolson method · Electron-wave interaction · Gyrotron

## 1 Introduction

Nowadays, one of the most promising high-powered vacuum tube is the gyrotron. To improve the gyrotron efficiency, complex models of an electron-wave interaction are required. In particular, it is important to take into account the influence of an electron beam on the structure of the electromagnetic field in the cavity, which leads to the need to solve self-consistent problems with a non-fixed field structure. In this paper, two models are considered: stationary and time-depended. The stationary model [1, 2] allows to quickly find the generation efficiency and the output radiation power under the assumption of a single-mode operation. Gyrotrons typically operate in a one  $TE_{mp}$  mode of a cylindrical cavity. Various transition processes are possible in a gyrotron, especially in cases of operating in modes with high azimuthal and radial indices. In this case, the

---

This work was supported by a subsidy for Russian Federation State Assignment (Topic No. 0030-2019-0019).

problem of mode competition from neighboring modes or modes operating at lower cyclotron harmonics plays a significant role. Of interest is the analysis of the gyrotron startup scenarios (taking into account the dependence of voltage, current, and other parameters of the device on time). Different regimes of mode interaction, self-modulation and stochastic regimes are also possible in gyrotrons. In all these cases, it is necessary to use complicated time-dependent model [1, 3]. At present, there is a sufficient number of code-packages for modeling an electron-wave interaction in gyrotrons. Examples of such programs are the code package GYRO1-3 developed by Borie and Dumbrajs [4], the Maryland Gyrotron (MAGY) code [5], the code-package EURIDICE developed at the National Technical University of Athens [6] and the gyrotron design toolbox GYROCOMPU developed at Wuhan National High Magnetic Field Center (China) [7]. Papers [4–7] are mainly devoted to the description of mathematical models, but aren't fully revealing numerical methods which were used. This paper is devoted to the description of the methods implemented in the code-package ANGEL developed at IAP RAS for calculating an electron-wave interaction and analyzing the competition of modes in gyrotrons.

## 2 Stationary Model

In the stationary and the time-dependent models, we assume that the cavity is formed by segments of circular (azimuthally symmetric) weakly irregular waveguides, the radius of which is close to the cutoff radius of the operating mode. A typical weakly irregular cavity profile of gyrotron is shown in Fig. 2a. An electron-wave interaction is considered in following both models on the interval  $[z_{in}, z_{out}]$ .

The equations describing an interaction of the electron beam with the eigenmodes of a cylindrical cavity can take into account the inhomogeneity of the static magnetic field, the spread of oscillatory velocities, and the spread of the leading centers of the electron trajectories. Electrons in the beam can be classified into several groups:  $N_\theta$  initial electron phases of entering the cavity,  $N_g$  groups with different oscillatory velocities (but with constant initial beam energy),  $N_R$  fractions with the radii of the leading centers of Larmor orbits (for simulation the misalignment of the beam and the magnetic field axis, wide beams, multi-beam systems etc.)

In the stationary model  $N_a = N_\theta \times N_g \times N_R$  pairs of equations of motion (for the transverse and longitudinal components of the electron momentum)

$$\frac{dp_c}{dz} = f_{p_c}(z, p_c, p_{\parallel}, F, F'), \quad \frac{dp_{\parallel}}{dz} = f_{p_{\parallel}}(z, p_c, p_{\parallel}) \quad (1)$$

and the equation for the electromagnetic field

$$\frac{d^2 F}{dz^2} + \kappa_{\parallel}^2(z) \cdot F = \mathcal{J}(z, \{p_c, p_{\parallel}\}) \quad (2)$$

are jointly solved with initial conditions

$$F(z_{in}) = F_{in}, \quad p_{\parallel}(z_{in}) = p_{\parallel,in}\{g\}, \quad p_c(z_{in}) = e^{i\theta_0} \cdot p_{\perp,in}\{g\}, \quad (3)$$

$$g = \frac{p_{\perp}}{p_{\parallel}}, \quad \theta_0 = 2\pi \frac{j_{\theta}}{N_{\theta}}, \quad j_{\theta} = \overline{1, N_{\theta}},$$

and boundary conditions

$$\frac{dF}{dz} - i\kappa_{\parallel}F = 0, \quad z = z_{in}; \quad \frac{dF}{dz} + i\kappa_{\parallel}F = 0, \quad z = z_{out}. \quad (4)$$

Here  $F$  is the normalized high-frequency field,  $p_c$  and  $p_z$  are the parameters describing the electron beam,  $z$  is the axial coordinate of the cavity. The values  $F$  and  $p_c$  are complex,  $p_z$  is real. The function  $\kappa_{\parallel}(z)$  is determined by the geometry of the cavity  $R(z)$ . Equations (1)–(2) are self-consistently integrated, Eq. (1) describes the influence of a high-frequency field on the parameters of the electron beam, Eq. (2) describes the longitudinal structure of the mode, which depends on the electron beam. The integration of the equations of motion together with the inhomogeneous string equation is carried out by the Runge-Kutta method of the 4th order. As a result of solving the Sturm—Liouville problem (1)–(4), the longitudinal structure of the field  $F(z)$  is obtained for the found values of the frequency  $\omega$  and the initial amplitude  $F_{in}$ . The search for the eigenvalues  $(\omega, F_{in})$  is carried out similarly to the method described in using the argument principle and further refinement of the solution by the two-dimensional Newton method. The parameters of the electron beam  $p_c$ ,  $p_{\parallel}$ , the right-hand sides of Eqs. (1)–(2)  $f_{p_c}$ ,  $f_{p_{\parallel}}$ ,  $\mathcal{J}$  are defined in Sect. 4.

### 3 Multimode Time-Depended Model

#### 3.1 Mathematical Formulation of the Problem

In the time-depended model  $N_a = N_{\psi} \times N_{\theta} \times N_g \times N_R$  pairs of equations of motion

$$\frac{\partial p_c}{\partial z} = f_{p_c}(z, p_c, p_{\parallel}, \{F_s\}), \quad \frac{\partial p_{\parallel}}{\partial z} = f_{p_{\parallel}}(z, p_c, p_{\parallel}), \quad (5)$$

and  $N_s$  equations for the field

$$\frac{\partial^2 F_s}{\partial z^2} + C_0 \frac{\partial F_s}{\partial \tau} + \kappa_{\parallel,s}^2(z) \cdot F_s = \mathcal{J}_s(z, \{p_c, p_{\parallel}\}) \quad (6)$$

are jointly solved with initial particle momenta (3), nonzero initial field  $F_s(z, 0) = F_{in,s}(z)$  and the nonreflective radiation boundary conditions at the bounds for each  $s$ -th mode

$$F(z_{in}, \tau) - C_1 \cdot \int_0^{\tau} \frac{\partial F(z_{in}, \partial \tilde{\tau})}{\partial z} \cdot \frac{e^{C_L \cdot (\tau - \tilde{\tau})}}{\sqrt{\tau - \tilde{\tau}}} \cdot d\tilde{\tau} = 0, \quad (7)$$

$$F(z_{out}, \tau) + C_1 \cdot \int_0^\tau \frac{\partial F(z_{out}, \partial \tilde{\tau})}{\partial z} \cdot \frac{e^{C_R \cdot (\tau - \tilde{\tau})}}{\sqrt{\tau - \tilde{\tau}}} \cdot d\tilde{\tau} = 0. \quad (8)$$

The system of Eq. (5)–(6) with boundary conditions (7)–(8) is solved in the rectangular region  $[z_{in}, z_{out}] \times [0, T_{fin}]$ . In (6)–(8)  $\tau$  is the normalized time. The use of equations in general form (5)–(8) is convenient for describing numerical methods. The specific expressions for the right parts  $f_{p_c}$ ,  $f_{p_{\parallel}}$ ,  $\mathcal{J}_s$ , the constants  $C_0$ ,  $C_1$ ,  $C_L$ ,  $C_R$  and other parameters are defined in Sect. 4.

### 3.2 Implicit Crank—Nicolson Scheme

To solve the system of Eqs. (5)–(6) by the finite difference method, the implicit Crank—Nicolson scheme [8, pp. 192–193] is used, which provides the second order of accuracy, but requires repeated solution of equations of motion at each time step, as well as solving SLAE by the tridiagonal matrix algorithm to find the field amplitude at each time layer. This numerical scheme uses the  $3 + 3$  stencil, that is, 3 nodes from the previous time layer and 3 nodes from the current layer (see Fig. 1).

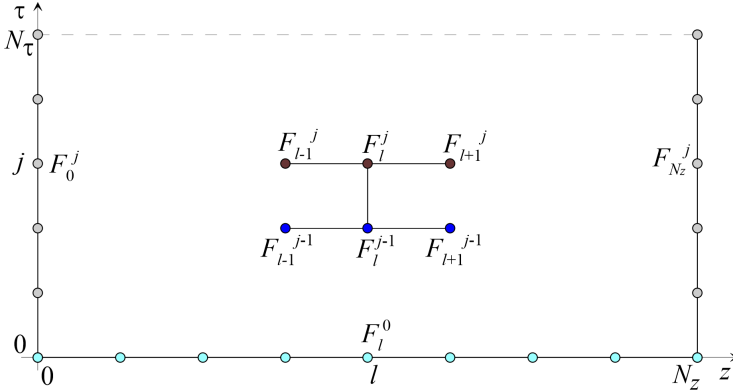


**Fig. 1.** The Crank—Nicolson stencil (3+3).

It is convenient to use a uniform grid in space and time

$$\{z_l, \tau^j\} \equiv \{z_{in} + \delta_z \cdot l, \delta_\tau \cdot j\}, \quad l = \overline{0, N_z}, \quad j = \overline{0, N_\tau};$$

$$\delta_z = \frac{(z_{out} - z_{in})}{N_z}, \quad \delta_\tau = \frac{T_{fin}}{N_\tau}.$$

The complex field amplitudes at grid nodes are denoted as  $F_l^j \equiv F_s(z_l, \tau^j)$ . The right-hand sides of the equation are denoted as  $f_l^j \equiv \mathcal{J}_s(z_l, \tau^j) - \kappa_{\parallel, s}^2(z_l) \cdot F_l^j$ . Approximation of derivatives:

$$\frac{\partial F}{\partial \tau}(z_l, \tau^j) \approx \frac{1}{\delta_\tau} \cdot (F_l^j - F_l^{j-1}), \quad (9)$$

$$\frac{\partial^2 F}{\partial z^2}(z_l, \tau^j) \approx \frac{1}{\delta_z^2} \cdot \left( F_{l-1}^j - 2 F_l^j + F_{l+1}^j \right), \quad (10)$$

$$\frac{\partial F}{\partial z}(z_l, \tau^j) \approx \frac{1}{\delta_z} \cdot \left( F_l^j - F_{l-1}^j \right) \approx \frac{1}{\delta_z} \cdot \left( F_{l+1}^j - F_l^j \right). \quad (11)$$

For internal nodes ( $z_{in} < z < z_{out}$ ) the approximation of Eq. (6) takes the form

$$\begin{aligned} \frac{C_0}{\delta_\tau} \cdot \left( F_l^j - F_l^{j-1} \right) = \frac{1}{2} \cdot \left( f_l^j + f_l^{j-1} \right) - \frac{1}{2\delta_z^2} \cdot \left( F_{l-1}^j \right. \\ \left. - 2 F_l^j + F_{l+1}^j + F_{l-1}^{j-1} - 2 F_l^{j-1} + F_{l+1}^{j-1} \right), \quad l = \overline{1, N_z - 1}. \end{aligned} \quad (12)$$

The link of boundary nodes with internal nodes is determined by boundary conditions for  $z_{in}$  and  $z_{out}$ . The result is a tridiagonal SLAE matrix

$$\mathcal{A} \cdot \mathbf{F} = \mathbf{d}, \quad (13)$$

$$\mathcal{A} = \begin{pmatrix} a_0 & b_0 & 0 & \cdots & & 0 & 0 \\ c_1 & a_1 & b_1 & 0 & \cdots & & 0 \\ 0 & c_2 & a_2 & b_2 & 0 & \cdots & 0 \\ \vdots & & & \ddots & & & \vdots \\ 0 & \cdots & 0 & c_{N_z-2} & a_{N_z-2} & b_{N_z-2} & 0 \\ 0 & & \cdots & 0 & c_{N_z-1} & a_{N_z-1} & b_{N_z-1} \\ 0 & 0 & \cdots & & 0 & c_{N_z} & a_{N_z} \end{pmatrix},$$

$$\mathbf{F} = \{F_l\}, \quad \mathbf{d} = \{d_l\}, \quad l = \overline{0, N_z}.$$

To bring to this form, it's suitable to rewrite the Eq. (12):

$$\begin{aligned} F_{l-1}^j + \left( 2 C_0 \frac{\delta_z^2}{\delta_\tau} - 2 \right) \cdot F_l^j + F_{l+1}^j = \delta_z^2 \cdot \left( f_F^j + f_F^{j-1} \right) + \\ + \left( 2 C_0 \frac{\delta_z^2}{\delta_\tau} + 2 \right) \cdot F_l^{j-1} - \left( F_{l-1}^{j-1} + F_{l+1}^{j-1} \right), \quad l = \overline{1, N_z - 1}. \end{aligned}$$

It is followed that for all columns of the matrix except the zero and the last, the elements are constant

$$a_l = 2 C_0 \frac{\delta_z^2}{\delta_\tau} - 2 = -2 \left( 1 - C_0 \frac{\delta_z^2}{\delta_\tau} \right), \quad b_l = c_l = 1, \quad l = \overline{1, N_z - 1},$$

and the corresponding elements of the right-hand side of the Eq. (13) have the form

$$d_l = \delta_z^2 \cdot \left( f_F^j + f_F^{j-1} \right) + 2 \left( 1 + C_0 \frac{\delta_z^2}{\delta_\tau} \right) \cdot F_l^{j-1} - \left( F_{l-1}^{j-1} + F_{l+1}^{j-1} \right).$$

The elements of the zero and last columns are determined by the boundary conditions.

If we approximate the derivative in the boundary conditions (7)–(8) using formula (11), the solution accuracy drops to  $O(\delta_z)$ , but using information about the structure of Eq. (6), we can increase the order of approximation of the derivative. Let's introduce the notation:

$$\sigma_l^j = \frac{1}{6} \cdot \frac{\partial^2 F}{\partial z^2}(z_l, \tau^j),$$

and write down the finite difference for Eq. (6) according to the Crank—Nicolson scheme only in time (9) similarly to Eq. (12), but keeping the second derivative unchanged:

$$\frac{C_0}{\delta_\tau} (F_l^j - F_l^{j-1}) = \frac{1}{2} (f_l^j + f_l^{j-1}) - 3 (\sigma_l^j + \sigma_l^{j-1}). \quad (14)$$

Next, it is used the spline representation of the first derivative from [9]. For the left and right bounds it has the form:

$$\begin{aligned} \frac{\partial F}{\partial z}(z_{in}, \tau^j) &= \frac{1}{\delta_z} \cdot (F_1^j - F_0^j) - \delta_z \cdot (2\sigma_0^j + \sigma_1^j), \\ \frac{\partial F}{\partial z}(z_{out}, \tau^j) &= \frac{1}{\delta_z} \cdot (F_{N_z}^j - F_{N_z-1}^j) + \delta_z \cdot (2\sigma_{N_z}^j + \sigma_{N_z-1}^j). \end{aligned} \quad (15)$$

Using the relation (14) for  $l = 0$  and  $l = 1$  the sum  $(2\sigma_0^j + \sigma_1^j)$  is expressed and substituted in (15a). The first derivative at the left bound for the left column of the SLAE matrix takes the form:

$$\begin{aligned} \frac{\partial F}{\partial z}(z_{in}, \tau^j) &= W_0 \cdot F_0^j + W_1 \cdot F_1^j + W_L, \\ W_0 &= \frac{2}{3} C_0 \frac{\delta_z}{\delta_\tau} - \frac{1}{\delta_z}, \quad W_1 = \frac{C_0}{3} \frac{\delta_z}{\delta_\tau} + \frac{1}{\delta_z}, \\ W_L &= -\delta_z \cdot \left\{ \frac{C_0}{3\delta_\tau} (2F_0^{j-1} + F_1^{j-1}) - (2\sigma_0^{j-1} + \sigma_1^{j-1}) \right. \\ &\quad \left. + \frac{1}{6} (2f_{F,0}^{j-1} + f_{F,1}^{j-1} + 2f_{F,0}^j + f_{F,1}^j) \right\}. \end{aligned}$$

Similarly, one finds the expression for  $(2\sigma_{N_z}^j + \sigma_{N_z-1}^j)$  in (15b) using the relation (14) with  $l = N_z$  and  $l = N_z - 1$  and gets the first derivative at the right bound for the right column in the form:

$$\begin{aligned} \frac{\partial F}{\partial z}(z_{out}, \tau^j) &= W_{N_z-1} \cdot F_{N_z-1}^j + W_{N_z} \cdot F_{N_z}^j + W_R, \\ W_{N_z-1} &= -\left( \frac{1}{\delta_z} + \frac{C_0}{3} \frac{\delta_z}{\delta_\tau} \right), \quad W_{N_z} = \left( \frac{1}{\delta_z} - \frac{2}{3} C_0 \frac{\delta_z}{\delta_\tau} \right), \\ W_R &= \delta_z \cdot \left\{ \frac{C_0}{3\delta_\tau} (2F_{N_z}^{j-1} + F_{N_z-1}^{j-1}) - (2\sigma_{N_z}^{j-1} + \sigma_{N_z-1}^{j-1}) \right. \\ &\quad \left. + \frac{1}{6} (2f_{N_z}^{j-1} + f_{N_z-1}^{j-1} + 2f_{N_z}^j + f_{N_z-1}^j) \right\}. \end{aligned} \quad (16)$$



### 3.3 Approximation of the Boundary Conditions

An additional difficulty is added by the singularity contained in the boundary conditions (7)–(8). The integral is split into the sum of integrals corresponding to the time steps:

$$\begin{aligned} \int_0^\tau \frac{\partial F(z_{in}, \tilde{\tau})}{\partial z} \cdot \frac{e^{C_L \cdot (\tau - \tilde{\tau})}}{\sqrt{\tau - \tilde{\tau}}} \cdot d\tilde{\tau} &= I_L + I_j(z_{in}), \\ \int_0^\tau \frac{\partial F(z_{out}, \tilde{\tau})}{\partial z} \cdot \frac{e^{C_R \cdot (\tau - \tilde{\tau})}}{\sqrt{\tau - \tilde{\tau}}} \cdot d\tilde{\tau} &= I_R + I_j(z_{out}), \\ I_L &= \sum_{\tilde{j}=1}^{j-1} I_{\tilde{j}}(z_{in}), \quad I_R = \sum_{\tilde{j}=1}^{j-1} I_{\tilde{j}}(z_{out}), \\ I_j(z_q) &= \int_{(\tilde{j}-1) \cdot \delta_\tau}^{\tilde{j} \cdot \delta_\tau} \frac{\partial F(z_q, \tilde{\tau})}{\partial z} \cdot \frac{e^{C_q \cdot (j \cdot \delta_\tau - \tilde{\tau})}}{\sqrt{j \cdot \delta_\tau - \tilde{\tau}}} \cdot d\tilde{\tau}, \\ C_q &= C_L, \quad z_q = z_{in}, \quad C_q = C_R, \quad z_q = z_{out}. \end{aligned}$$

The following analytical calculations are given for the boundary condition (8). Similar calculations can be repeated for the boundary condition (7). The integrand of each  $I_{\tilde{j}}$  is linearized in  $\tilde{\tau}$  only the derivative and the exponent; the integrals of  $(\tau - \tilde{\tau})^{-1/2}$  and  $\tilde{\tau}/\sqrt{\tau - \tilde{\tau}}$  are taken analytically:

$$\begin{aligned} I_{\tilde{j}} &\approx \tilde{I}_{\tilde{j}} = a_{\tilde{j}} I_{\tilde{j}}^a + b_{\tilde{j}} I_{\tilde{j}}^b, \\ a_{\tilde{j}} &= \frac{1}{\delta_\tau} (\tilde{\tau}_{\tilde{j}} u_{\tilde{j}-1} - \tilde{\tau}_{\tilde{j}-1} u_{\tilde{j}}) = (\tilde{j} \cdot u_{\tilde{j}-1} - (\tilde{j}-1) \cdot u_{\tilde{j}}), \\ b_{\tilde{j}} &= \frac{u_{\tilde{j}} - u_{\tilde{j}-1}}{\delta_\tau}, \quad u_{\tilde{j}} = \frac{\partial F(z_{out}, \tilde{\tau})}{\partial z} \cdot e^{C_R \cdot (\tau - \tilde{\tau})}, \\ I_{\tilde{j}}^a &= \int_{\tau_{\tilde{j}} - \delta_\tau}^{\tau_{\tilde{j}}} \frac{d\tilde{\tau}}{\sqrt{\tau - \tilde{\tau}}} = \int_{(\tilde{j}-1) \cdot \delta_\tau}^{\tilde{j} \cdot \delta_\tau} \frac{d\tilde{\tau}}{\sqrt{j \cdot \delta_\tau - \tilde{\tau}}} \\ &= -2\sqrt{\tau - \tilde{\tau}} \Big|_{(\tilde{j}-1) \cdot \delta_\tau}^{\tilde{j} \cdot \delta_\tau} = -2\sqrt{\delta_\tau} \left\{ \sqrt{j - \tilde{j}} - \sqrt{j - \tilde{j} + 1} \right\}, \\ I_{\tilde{j}}^b &= \int_{\tau_{\tilde{j}} - \delta_\tau}^{\tau_{\tilde{j}}} \frac{\tilde{\tau} d\tilde{\tau}}{\sqrt{\tau - \tilde{\tau}}} = \int_{(\tilde{j}-1) \cdot \delta_\tau}^{\tilde{j} \cdot \delta_\tau} \frac{\tilde{\tau} d\tilde{\tau}}{\sqrt{j \cdot \delta_\tau - \tilde{\tau}}} = \left\{ \frac{2}{3} (\tau - \tilde{\tau})^{3/2} - 2\tau \sqrt{\tau - \tilde{\tau}} \right\} \Big|_{(\tilde{j}-1) \cdot \delta_\tau}^{\tilde{j} \cdot \delta_\tau} \end{aligned}$$

$$= \frac{2}{3} \delta_\tau^{3/2} \left\{ (j - \tilde{j})^{3/2} - (j - \tilde{j} + 1)^{3/2} \right\} - 2j \delta_\tau^{3/2} \left\{ \sqrt{j - \tilde{j}} - \sqrt{j - \tilde{j} + 1} \right\}.$$

As a result, we obtain

$$\begin{aligned} \tilde{I}_{\tilde{j}} = & \frac{4}{3} \sqrt{\delta_\tau} \left\{ u_{\tilde{j}-1} \cdot \left[ (j - \tilde{j}) \sqrt{j - \tilde{j}} - \left( j - \tilde{j} - \frac{1}{2} \right) \sqrt{j - \tilde{j} + 1} \right] \right. \\ & \left. + u_{\tilde{j}} \cdot \left[ (j - \tilde{j} + 1) \sqrt{j - \tilde{j} + 1} - \left( j - \tilde{j} + \frac{3}{2} \right) \sqrt{j - \tilde{j}} \right] \right\}. \end{aligned}$$

Special cases:

$$I_R \equiv 0, \quad j = 0, 1.$$

For  $j = 2$ , the case is already quite regular, but the sum contains only one term:

$$I_R = \tilde{I}_1 = \frac{4}{3} \sqrt{\delta_\tau} \left\{ u_0 \cdot \left( 1 - \frac{\sqrt{2}}{2} \right) + u_1 \cdot \left( 2\sqrt{2} - \frac{5}{2} \right) \right\}.$$

To speed up the summation, it is better to reorder the terms to minimize the access to the tables  $\frac{\partial F(z_{out}, \tilde{\tau})}{\partial z}$  and  $e^{C_R \cdot (\tau - \tilde{\tau})}$ . Square roots of integers in the range from 2 to the final time step number  $N_\tau$  are calculated once per calculation and are also kept in the tables  $\frac{\partial F(z_{out}, \tilde{\tau})}{\partial z}$  and  $e^{C_R \cdot (\tau - \tilde{\tau})}$ . For  $j > 2$ , we obtain

$$\begin{aligned} I_R = & \frac{4}{3} \sqrt{\delta_\tau} \left\{ u_0 \cdot \left[ (j - 1)^{3/2} - \left( j - \frac{3}{2} \right) \sqrt{j} \right] + u_{j-1} \cdot \left[ 2\sqrt{2} - \frac{5}{2} \right] \right. \\ & \left. + \sum_{\tilde{j}=1}^{j-2} u_{\tilde{j}} \cdot \left[ (j - \tilde{j} - 1)^{3/2} - 2(j - \tilde{j})^{3/2} + (j - \tilde{j} + 1)^{3/2} \right] \right\}. \end{aligned}$$

It is possible to further increase the accuracy of approximation of the integral  $I_{\tilde{j}}$  (or increase the integration step  $\delta_\tau$ , while maintaining accuracy) using the Fresnel integrals.

Using the refined representation of the derivative (16) and the method of eliminating the singularity in the integral  $I_j$  described above, one obtains the boundary conditions (7)–(8) in the form

$$\begin{aligned} F_0^j - C_1 \cdot \left( I_L + \frac{4}{3} \sqrt{\delta_\tau} \frac{\partial F}{\partial z}(z_{in}, \tau) + \frac{2}{3} \delta_\tau \frac{\partial F}{\partial z}(z_{in}, \tau - \delta_\tau) \cdot \frac{e^{C_L \cdot \delta_\tau}}{\sqrt{\delta_\tau}} \right) &= 0, \\ F_{N_z}^j + C_1 \cdot \left( I_R + \frac{4}{3} \sqrt{\delta_\tau} \frac{\partial F}{\partial z}(z_{out}, \tau) + \frac{2}{3} \delta_\tau \frac{\partial F}{\partial z}(z_{out}, \tau - \delta_\tau) \cdot \frac{e^{C_R \cdot \delta_\tau}}{\sqrt{\delta_\tau}} \right) &= 0, \end{aligned}$$

The elements of the SLAE matrix corresponding to the boundary conditions take the following form

$$a_0 = a_{N_z} = 1 - \frac{4}{3} C_1 W_0 \sqrt{\delta_\tau}, \quad b_0 = c_{N_z} = -\frac{4}{3} C_1 W_1 \sqrt{\delta_\tau}, \quad (17)$$

$$d_0 = C_1 \cdot \left( I_L + \frac{4}{3} W_L \sqrt{\delta_\tau} + \frac{2}{3} \delta_\tau \frac{\partial F}{\partial z}(z_{in}, \delta_\tau \cdot (j-1)) \cdot \frac{\exp(C_L \cdot \delta_\tau)}{\sqrt{\delta_\tau}} \right),$$

$$d_{N_z} = -C_1 \cdot \left( I_R + \frac{4}{3} W_R \sqrt{\delta_\tau} + \frac{2}{3} \delta_\tau \frac{\partial F}{\partial z}(z_{out}, \delta_\tau \cdot (j-1)) \cdot \frac{\exp(C_R \cdot \delta_\tau)}{\sqrt{\delta_\tau}} \right).$$

The result is a tridiagonal SLAE matrix, the right side of which contains combinations of field values from the previous time layer  $F^{j-1}$ . Solving this SLAE by the tridiagonal matrix algorithm, it is possible in  $O(N_z)$  operations to find the values of the nodes  $F_l^j$ ,  $l = \overline{0, N_z}$ .

The implicit dependences between the field and particle momenta can be resolved at each time step in several iterations. First, the equations of motion are solved in the field on the previous layer and  $\mathcal{J}[F^{j-1}]$  is found, after this, using (12)–(17), the SLAE is composed and solved, and thus the non-self-consistent field is found on the current layer  $\tilde{F}_l^j$ . Then, the equations of motion are again solved and  $\mathcal{J}[\tilde{F}^j]$  is obtained, and already with such a right-hand side, a self-consistent field is found in the same way on the current layer  $F_l^j$ .

## 4 Examples of Mode Competition in Gyrotrons Operating in Different Frequency Ranges

The algorithms described in this article are implemented in the code-package ANGEL (Analyzer of a Gyrating Electrons), which is written in FORTRAN-90 and used at IAP RAS and GYCOM Ltd. Previously, this code-package was used to simulate electron-optical systems of gyrotrons [10]. Implementation described above complex algorithms in the code-package ANGEL allows to simulate the electron-wave interaction in gyrotrons. The stationary model affords to determine the efficiency and output power in the single-mode operation. The multi-mode time-dependend self-consistent model allows to analyze transition processes, to investigate various dynamic and self-modulation regimes of generation. The described calculation methods can be used to investigate various effects in the gyrotron.

For modeling an electron-wave interaction in gyrotrons by the stationary model, the specific expressions for the right parts  $f_{p_c}$ ,  $f_{p_\parallel}$ ,  $\mathcal{J}_s$  of the Eq. (1)–(2) take the form:

$$f_{p_c} = -i \frac{p_c}{p_\parallel} \cdot \left( \gamma \frac{\kappa}{n} - \frac{\omega_{H_0}}{c} \right) + \kappa_\perp \cdot J_{m-n}(\kappa_\perp R_b) \cdot \frac{i\gamma F}{p_\parallel} \cdot (p_c^*)^{n-1} \cdot \left( \frac{J_{n-1}(\xi)}{2p_\perp^{n-1}} \right) + \frac{p_c}{2B_0} \cdot \frac{dB_0}{dz},$$

$$f_{p_\parallel} = -\frac{p_\perp^2}{p_\parallel \cdot 2B_0} \cdot \frac{dB_0}{dz},$$

$$\mathcal{J} = I \cdot \kappa \cdot \kappa_\perp \cdot \left\langle \left\langle J_{m-n}(\kappa_\perp R_b) \cdot \frac{p_c^n}{p_\parallel} \cdot \left( \frac{J'_n(\xi)}{p_\perp^{n-1}} \right) \right\rangle \right\rangle.$$

Here  $\gamma(z) = \sqrt{1 + p_\perp^2 + p_\parallel^2}$  is the Lorentz factor,  $\gamma_0 = \gamma(z_{in})$ ,  $p_\perp = \gamma \frac{v_\perp}{c}$ ,  $p_\parallel = \gamma \frac{v_\parallel}{c}$  are the normalized transverse and longitudinal momenta of electrons in a helical beam,  $n$  is the number of the cyclotron harmonic,  $\kappa$  is the wave number,  $\kappa_\perp$  and  $\kappa_\parallel$  are the transverse and longitudinal wave numbers,  $\omega_{H_0}$  is the nonrelativistic gyrofrequency,  $B_0$  is the external magnetic field,  $R_b$  is the average radius of the leading centers of electron orbits,  $J_m$  is the Bessel function,  $\xi(z) = \frac{\kappa_\perp c}{\omega_{H_0}} p_\perp$ ,  $I = \frac{C_I \cdot I_b}{(\nu_{m,p}^2 - m^2) \cdot J_m^2(\nu_{m,p})}$  is the normalized beam current,  $C_I = \frac{8 e_0}{c m_0} \cdot 10^{-7} \approx 0.4693 \cdot 10^{-3}$ ,  $I_b$  is the beam current in amperes.

In the case of the multimode time-depended model, the expressions for the right parts of the equations different and take the form:

$$\begin{aligned}
 f_{p_c} &= -i \frac{p_c}{p_\parallel} \cdot \left( \gamma \frac{\omega_p}{c} - \frac{\omega_{H_0}}{c} \right) + \frac{p_c}{2 B_0} \cdot \frac{dB_0}{dz} \\
 &+ i \sum_{s=1}^{N_s} \left\{ J_{m_s-n_s}(\kappa_{\perp,s} R_b) \cdot \frac{\gamma \kappa_{\perp,s}}{p_\parallel} \cdot (p_c^*)^{n_s-1} \cdot \left( \frac{J_{n_s-1}(\xi)}{2 p_\perp^{n_s-1}} \right) \cdot F_s e^{i(\Delta_s \tilde{z} + \psi_s)} \right\}, \\
 \mathcal{J}_s &= I_s \cdot \kappa_s \cdot \kappa_{\perp,s} \cdot \left\langle \left\langle J_{m_s-n_s}(\kappa_{\perp,s} R_b) \cdot \frac{p_c^{n_s}}{p_\parallel} \cdot \left( \frac{J'_{n_s}(\xi)}{p_\perp^{n_s-1}} \right) \cdot e^{-i(\Delta_s \tilde{z} + \psi_s)} \right\rangle \right\rangle, \\
 \Delta_s &= \frac{(\omega_s - n_s \omega_p)}{c \beta_\parallel}, \quad \psi_s = \left( \frac{m_1}{n_1} \cdot n_s - m_s \right) \cdot \psi_0, \quad \psi_0 = [0, 2\pi), \\
 \tau &= \frac{t \cdot c^2}{2 \cdot \omega_p}, \quad \kappa_{\perp,s} = \frac{\nu_{m_s, p_s}}{R_r(z)}, \quad \kappa_{\parallel,s}^2 = \kappa_s^2 - \kappa_{\perp,s}^2 \cdot \left( 1 + \frac{i}{Q_{ohm,s}} \right), \\
 \tilde{z} &= z - z_{in}, \quad \kappa_s = \frac{\omega_s}{c}. \quad C_0 = -i n_s.
 \end{aligned}$$

Here  $\omega_p$  is the averaging frequency, usually defined as  $\omega_1/n_1$  ( $s=1$  is index of the operating mode),  $\omega_s$  is the reference frequency of  $s$ -th mode. The sign  $\langle \dots \rangle$  means averaging in initial phases  $\theta_0$ , in angles  $\psi_0$ , in groups with different pitch factor  $g$  and in fractions with the radii of the leading centers of Larmor orbits  $R_b$ .

The constants  $C_1$ ,  $C_L$ ,  $C_R$  in the nonreflective radiation boundary conditions (7)–(8) are following

$$C_1 = \frac{e^{-i\pi/4}}{\sqrt{\pi \cdot n_s}}, \quad C_L = -\frac{i}{n_s} \cdot \kappa_{\parallel,s}^2(z_{in}), \quad C_R = -\frac{i}{n_s} \cdot \kappa_{\parallel,s}^2(z_{out}).$$

As an example of using these algorithms, we illustrate the impact of ohmic losses on the efficiency and stability of the gyrotron operation at high cyclotron harmonics under the condition of strong competition from spurious modes. The transition to operation at high cyclotron harmonics allows to reduce the external magnetic field by  $n$  times. It expands a number of gyrotron applications

[11]. Two versions of gyrotron operating at 30 GHz (the low-frequency version) and 500 GHz (the high-frequency version) are considered. They have the same operating parameters (accelerating voltage 15 kV and current 0.5 A) and scalable dimensions of the electrodynamic system. For example, the  $TE_{28,3}$  mode at the second cyclotron harmonic was selected as an operating mode. In this case the nearest spurious mode is the  $TE_{-10,3}$  mode, operating at the fundamental cyclotron resonance. It should be noted that the version of a gyrotron with the operating mode at 30 GHz is practically infeasible due to the large size of the electrodynamic system. Nevertheless, the chosen mode is typical in the case of terahertz gyrotrons and has the problem of mode competition, which is specific issue of gyrotrons of this range.

The ohmic quality factor (ohmic  $Q$ -factor) is introduced into the system of equations through the longitudinal wave number  $\kappa_{||}$ . For each gyrotron versions, the length of interaction space and the magnetic field were optimized to achieve the maximum efficiency of the operating mode. Figure 2a shows the calculated distributions of the high-frequency field along the interaction space of the operating mode and the spurious mode. The  $TE_{28,3}$  mode has a similar to gaussian structure with a high diffraction  $Q$ -factor, corresponding to the optimal electron-wave interaction; then the  $TE_{-10,3}$  mode is traveling wave and has a longitudinal structure with several variations of the RF field and respectively a lower diffraction  $Q$ -factor. Figure 2b shows the typical dependence of the efficiency on the generation frequency of these modes. With an increase in the generation frequency of the operating mode from 30 GHz to 1000 GHz, the calculated efficiency decreases from 11.35% to 1.77%; while ohmic losses practically do not affect the efficiency of the spurious mode.

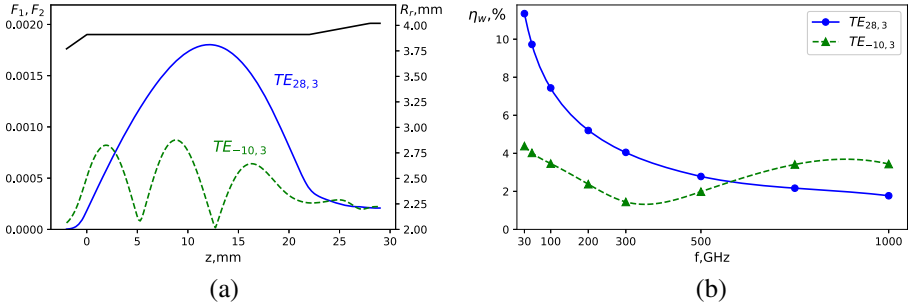


**Fig. 2.** (a) Example of a cavity profile and longitudinal structures of modes. (b) The gyrotron efficiency as a function of the generation frequency of the  $TE_{28,3}$  mode.

The multimode time-dependent self-consistent model allows to analyze the stability of  $TE_{28,3}$  and  $TE_{-10,3}$  modes in this frequency range. Figure 3 shows the time dependence of the mode amplitudes with the optimal initial operating mode amplitude and small amplitude of spurious mode. Figure 4 shows the planes of dimensionless amplitudes of the fields of the operating and spurious modes for

the low-frequency (Fig. 4a) and the high-frequency (Fig. 4b) gyrotron versions. In the case of the low-frequency version the operating mode has stable generation. With an increase in the generation frequency and, accordingly, the fraction of ohmic losses in the cavity, the “saddle point” come up to the equilibrium point “stable node” corresponding to the single-mode operation. In the case of a high-frequency gyrotron, the operating mode turns unstable due to the bifurcation of equilibrium points. The generation of radiation on the spurious mode remains stable in the entire frequency range.

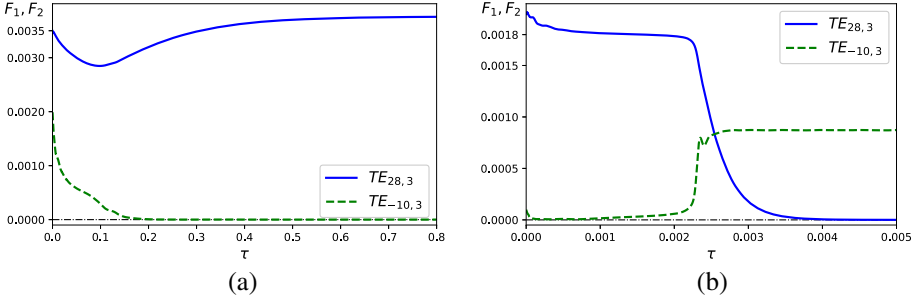


**Fig. 3.** Time dependence of the amplitudes  $F_1$  and  $F_2$  of the  $TE_{28,3}$  and the  $TE_{-10,3}$  modes respectively, obtained with the multimode time-dependent self-consistent model. (a) The low-frequency version. (b) The high-frequency version.

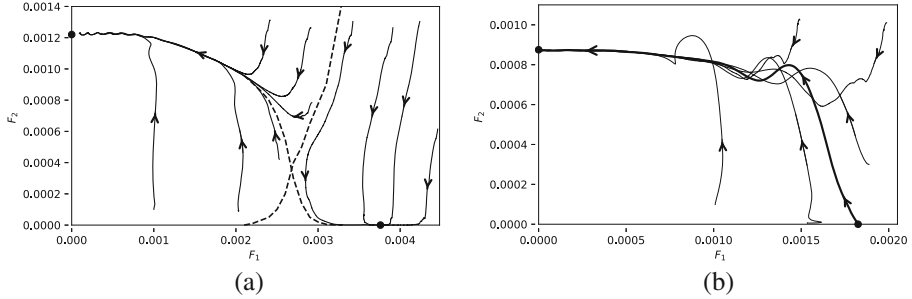


**Fig. 4.** Planes of amplitudes of the operating and the spurious modes. (a) The low-frequency version. (b) The high-frequency version.

The ratio of the total  $Q$ -factor of the spurious mode to the total  $Q$ -factor of the operating mode is essential for the stability of the gyrotron operation. In the case of the low-frequency gyrotron version the contribution of the ohmic  $Q$ -factor to the total  $Q$ -factor is negligible, then the parameter is determined mainly by the ratio of the diffraction  $Q$ -factors. In the case of the high-frequency

gyrotron version, due to an increase in the fraction of ohmic losses, the parameter increases by 2.3 times relative to the low-frequency gyrotron version, which leads to a significant decrease in the stability of the operating mode.

In the calculations, the number of points along the axis  $z$  was equal to 200, the number of initial phases  $N_\theta$  was equal to 57, the number groups with different oscillatory velocities  $N_g$  was equal to 37, the number of azimuthal angle  $N_\psi$  was equal to 37. Only one fraction with the optimal radii of the leading centers was considered. This corresponds to calculating the gyrotron efficiency with stationary model for a split second and calculating the mode competition using the time-dependent model for several hours (the number of time steps was equal to about 20000).

## 5 Conclusion

The paper presents the stationary and the multimode time-dependent models designed to calculate the electron-wave interaction in gyrotron cavity and implemented in the code-package ANGEL. Used numerical methods are described in details. The approach of refined representation of the first derivative by using information about the structure of the Schrödinger equation is applied to increase the solution accuracy. The method of eliminating the singularity in the integral of the nonreflective radiation boundary condition is shown.

The calculations showed that the main problem of terahertz gyrotrons is the problem of realizing the stable single-mode operation at high cyclotron harmonics, which, as a rule, is solved by choosing the operating mode, the parameters of the electron beam and the electrodynamic system, as well as using various methods of additional selection of the operating mode.

**Acknowledgments.** The authors are grateful to prof. A.S. Sergeev for his valuable pieces of advice. This work was supported by a subsidy for Russian Federation State Assignment (Topic No. 0030-2019-0019).

## References

1. Moiseev, M.A., Nemirovskaya, L.L., Zapevalov, V.E., Zavolsky, N.A.: Numerical simulation of mode interaction in 170 GHz/1 MW gyrotrons for ITER. *Int. J. Infrared Millimeter Waves* **18**, 2117–2128 (1997). <https://doi.org/10.1007/BF02678254>
2. Moiseev, M.A., Zapevalov, V.E., Zavolsky, N.A.: Efficiency enhancement of the relativistic gyrotron. *Int. J. Infrared Millimeter Waves* **22**, 813–833 (2001). <https://doi.org/10.1023/A:1014954012067>
3. Ginzburg, N.S., Zavol'skii, N.A., Nusinovich, G.S., Sergeev, A.S.: Self-oscillation in UHF generators with diffraction radiation output. *Radiophys. Quantum Electron.* **29**, 89–97 (1986). <https://doi.org/10.1007/BF01034008>
4. Dumbrajs, O., Borie, E.: Calculation of eigenmodes of tapered gyrotron resonators. *Int. J. Electron.* **60**, 143–154 (1986). <https://doi.org/10.1080/00207218608920768>

5. Botton, M., Antonsen, T.M., Levush, B., Nguyen, K.T., Vlasov, A.N.: MAGY: a time-dependent code for simulation of slow and fast microwave sources. *IEEE Trans. Plasma Sci.* **26**, 882–892 (1998). <https://doi.org/10.1109/27.700860>
6. Avramides, K.A., Pagonakis, I.Gr., Iatrou, C.T., Vomvouridis, J.L.: EURIDICE: a code-package for gyrotron interaction simulations and cavity design. In: *EPJ Web of Conferences*, vol. 32, p. 04016 (2012). <https://doi.org/10.1051/epjconf/20123204016>
7. Wang, P., Chen, X., Xiao, H., Dumbrajs, O., Qi, X., Li, L.: GYROCOMPU: toolbox designed for the analysis of gyrotron resonators. *IEEE Trans. Plasma Sci.* **48**, 3007–3016 (2020). <https://doi.org/10.1109/TPS.2020.3013299>
8. Richtmyer, R.D., Morton, K.W.: *Difference Methods for Initial-Value Problems*, 2nd edn. Interscience Publishers, New York (1967)
9. Forsythe, G.E., Malcolm, M.A., Moler, C.B.: *Computer Methods for Mathematical Computations*. Prentice Hall, Englewood Cliffs (1977)
10. Plankin, O.P., Semenov, E.S.: Trajectory analysis of the electronic-optical system technological gyrotron. *Vestnik Novosib. Gos. Univ. Ser. Fiz.* **8**, 44–54 (2013). [in Russian]
11. Glyavin, M.Yu., Idehara, T., Sabchevski, S.P: Development of THz gyrotrons at IAP RAS and FIR UF and their applications in physical research and high-power THz technologies. *IEEE Trans. Terahertz Sci. Technol.* **5**, 788–797 (2015). <https://doi.org/10.1109/TTHZ.2015.2442836>